Materials Today Energy 25 (2022) 100985

Contents lists available at ScienceDirect

Materials Today Energy

journal homepage: www.journals.elsevier.com/materials-today-energy/

Enhanced thermoelectric performance in SnTe due to the energy filtering effect introduced by Bi_2O_3

Tao Hong [a], Changrong Guo [a], Dongyang Wang [a], Bingchao Qin [a], Cheng Chang [b, *], Xiang Gao [c, **], Li-Dong Zhao [a, ***]

[a] School of Materials Science and Engineering, Beihang University, Beijing, 100191, China
[b] Institute of Science and Technology Austria, Am Campus 1, 3400, Klosterneuburg, Austria
[c] Center for High Pressure Science and Technology Advanced Research (HPSTAR), Beijing, 100094, China

ARTICLE INFO

Article history:
Received 1 February 2022
Received in revised form
25 February 2022
Accepted 4 March 2022
Available online 10 March 2022

Keywords:
Eco-friendly thermoelectric material
Tin telluride
Bi_2O_3
Nanoprecipitates
Energy filtering effect

ABSTRACT

SnTe is a promising Pb-free thermoelectric (TE) material with high electrical conductivity. We discovered the synergistic effect of Bi_2O_3 on enhancing the average power factor (*PF*) and overall *ZT* value of the SnTe-based thermoelectric material. The introduction of Bi_2O_3 forms plenty of SnO_2, Bi_2O_3, and Bi-rich nanoprecipitates. These interfaces between the SnTe matrix and the nanoprecipitates can enhance the average *PF* through the energy filtering effect. On the other hand, abundant and diverse nanoprecipitates can significantly diminish the lattice thermal conductivity (κ_{lat}) through enhanced phonon scattering. The synergistic effect of Bi_2O_3 resulted in a maximum *ZT* (ZT_{max}) value of 0.9 at SnTe-2% Bi_2O_3 and an average *ZT* (ZT_{ave}) value of 0.4 for SnTe-4% Bi_2O_3 from 300 K to 823 K. The work provides an excellent reference to develop non-toxic high-performance TE materials.

1. Introduction

Due to the increasing energy shortage crisis, scientific researchers are eager to find new energy sources and technologies. TE materials can convert heat into electricity directly, providing a promising path to easing the fossil energy shortage [1–6]. Thermoelectric materials have been widely applied to various fields, such as waste heat recovery, deep space probes, wearable devices, chip cooling. The energy conversion efficiency of TE materials can be evaluated by the figure-of-merit ZT, $ZT = \sigma S^2 T/(\kappa_{ele}+\kappa_{lat})$, where σ is the electrical conductivity; S is the Seebeck coefficient; T is the Calvin temperature; κ_{ele} is the electronic thermal conductivity; κ_{lat} is the lattice thermal conductivity. In order to achieve high thermoelectric performance, it is necessary to obtain high *PF* while possessing low thermal conductivity. However, these parameters are closely coupled with each other, and the optimization of one parameter usually leads to the deterioration of the other parameters [7–13].

SnTe, an analog of PbTe without the toxic element Pb, is well-known for the extensive intrinsic Sn vacancies, which results in the high hole carrier concentration (n) and high κ_{tot}, providing a great challenge to optimize the TE performance [14–17]. Previous researchers have taken several approaches to improve the electrical transport properties of SnTe-based materials, such as optimizing n to reduce σ [18–20] and adjusting the energy band structure to increase S [21–23]. On the other hand, the thermal transport properties can be optimized by introducing defects with different scales because the second phase will form different scales of precipitates embedded in the matrix to enhance the phonon scattering [24–26], such as point defects [27,28], nanoprecipitates [29,30], and hierarchical architectures [31,32]. The thermal reduction effect in SnTe system has been confirmed by nanoprecipitates such as CdS [33], ZnS [30], CdTe [34], SrTe [35], ZnO [36], $AgSbTe_2$ [37], $AgBiTe_2$ [38], $AgSbSe_2$ [39], *etc.*

In this work, we introduced Bi_2O_3 into the SnTe matrix. We found that the nanoprecipitates in SnTe—Bi_2O_3 led to decreased n and enhanced S due to the energy filtering effect. We also prepared a series of SnTe-x% Bi for comparison. Comparing the two SnTe series, we found that it was not the extra Bi but the interfaces

* Corresponding author.
** Corresponding author.
*** Corresponding author.
E-mail addresses: cheng.chang@ist.ac.at (C. Chang), xiang.gao@hpstar.ac.cn (X. Gao), zhaolidong@buaa.edu.cn (L.-D. Zhao).

https://doi.org/10.1016/j.mtener.2022.100985
2468-6069/

between the oxide nanoprecipitates and SnTe that contributed to the high S and low κ. Specifically, the incoherent interfaces formed high potential barriers suppressing the low-energy carrier transport. Moreover, the nanoprecipitates reduced κ_{lat} significantly due to the phonon scattering. As a result, the ZT_{max} value reached 0.9 at 823 K for SnTe-2% Bi_2O_3, and the ZT_{ave} value reached 0.40 at 300−823 K for SnTe-4% Bi_2O_3.

2. Results and discussion

Fig. 1(a, b) showed the powder X-ray diffraction (XRD) patterns of SnTe-x% Bi (x = 0−8%) and SnTe-y% Bi_2O_3 (y = 0−4%) samples. As Bi content increased, there were no additional diffraction peaks found in the cubic structure ($Fm\bar{3}m$). But it was noteworthy that the diffraction peak of the SnO_2 and Bi_2O_3 second phase appeared when y≥2 with increasing Bi_2O_3 contents. It is well-known that the electronegativity of Sn (1.477) element is smaller than that of Bi (2.342), indicating that SnO_2 was derived from the reaction between Sn and Bi_2O_3 during the high-temperature solid-phase reaction. As shown in Fig. 1(c, d), the lattice parameters increased and then remained constant with increasing Bi/Bi_2O_3 amounts, indicating that some Bi atoms occupied Sn vacancies or substituted Sn atoms. Figs. S1 and S2 depicted the scanning electron microscopy (SEM) characterization results obtained from the ground and polished samples, including secondary electron images, backscattered electron images, and the elemental analysis results of SnTe-2% Bi_2O_3 and SnTe-4% Bi_2O_3, respectively. In SnTe-2% Bi_2O_3, the constituent elements are uniformly distributed in the sample. And a large number of Bi-enriched second phases appeared in the SnTe-4% Bi_2O_3 sample, which was consistent with the XRD results in Fig. 1.

Fig. 2(a-b) represents curves of the temperature-dependent electrical conductivity (σ) of SnTe−Bi and SnTe−Bi_2O_3. It can be seen that the decrease of σ is non-significant with the 1−8% Bi addition in Fig. 2(a). σ dropped from 8965 S cm^{-1} for intrinsic SnTe to 6746 S cm^{-1} for x = 8% at 300 K. However, for SnTe-y% Bi_2O_3, σ in the entire temperature region declined significantly with increasing Bi_2O_3 amounts, from 8965 S cm^{-1} for intrinsic SnTe to 2913 S cm^{-1} for SnTe-4% Bi_2O_3 at 300 K and from 977 S cm^{-1} to 642 S cm^{-1} at 823 K.

To illustrate the effect of excess Bi and Bi_2O_3 on the electrical properties of the SnTe matrix, we measured the hall carrier concentration (n_H) and carrier mobility (μ_H) at room temperature. As seen in Fig. 2(c), The addition of Bi caused a significant decrease in n_H at room temperature. However, when more Bi was added, n_H remained unchanged, indicating that excess Bi atoms did not significantly affect n_H. On the other hand, μ_H also increased firstly and then remained almost constant. Unlike SnTe-x% Bi, n_H and μ_H in SnTe-y% Bi_2O_3 kept decreasing with the increasing Bi_2O_3 amount in Fig. 2(d). The Seebeck coefficient (S) varying with temperature is demonstrated in Fig. 2(e−f). S in all samples increased with rising temperature. We found a distinct difference of S between SnTe-x% Bi and SnTe-y% Bi_2O_3. S in SnTe-x% Bi showed a significant increase over the entire temperature range compared to the pristine SnTe but did not increase further with rising Bi amounts. On the other hand, S in SnTe-x% Bi increased gradually with rising Bi_2O_3 amounts.

To investigate the origins of the high S, Pisarenko curves with different effective masses (m^*) were obtained based on the single parabolic band model. In Fig. 3(a), m^* was boosted by Bi doping from 0.079m_e for pristine SnTe to 0.19m_e for the SnTe-x% Bi samples and remained unchanged with the rising Bi amount. However, m^*

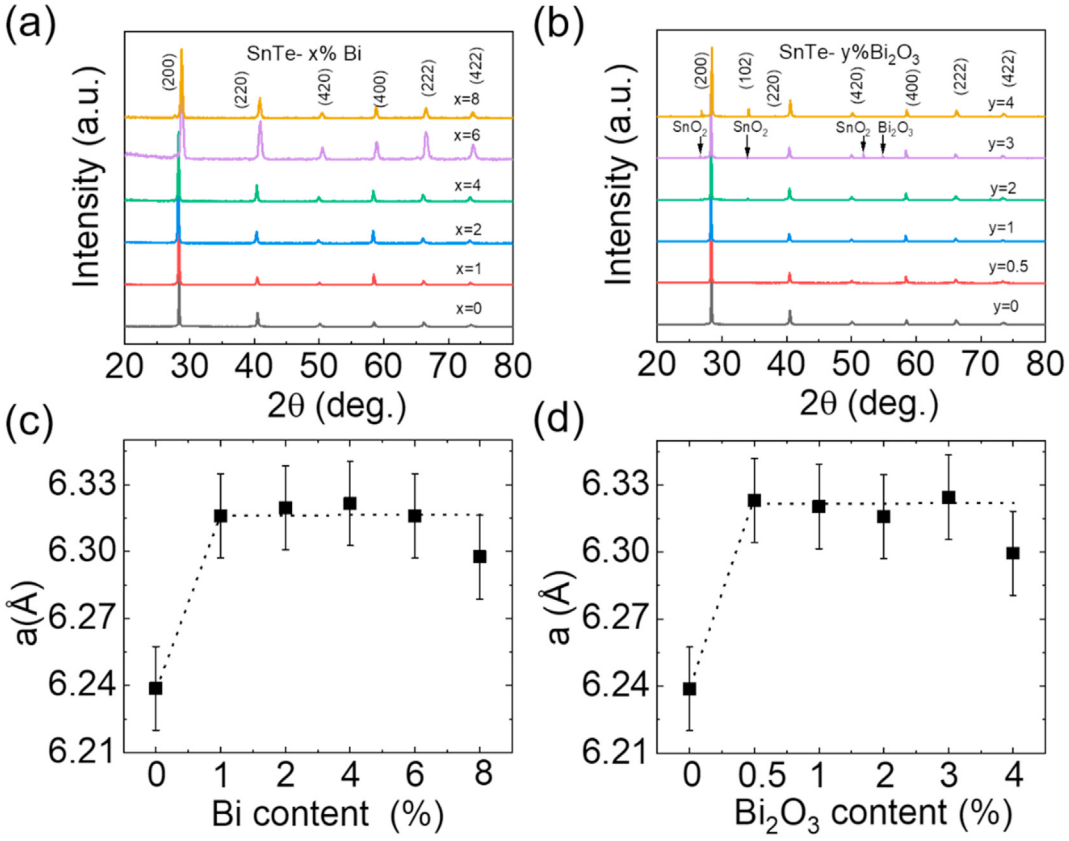

Fig. 1. Powder X-ray diffraction patterns of (a) SnTe-x% Bi (x = 0−8%) and (b) SnTe-y% Bi_2O_3 (y = 0−4%) samples; and the corresponding lattice parameters of (c) SnTe-x% Bi and (d) SnTe-y% Bi_2O_3.

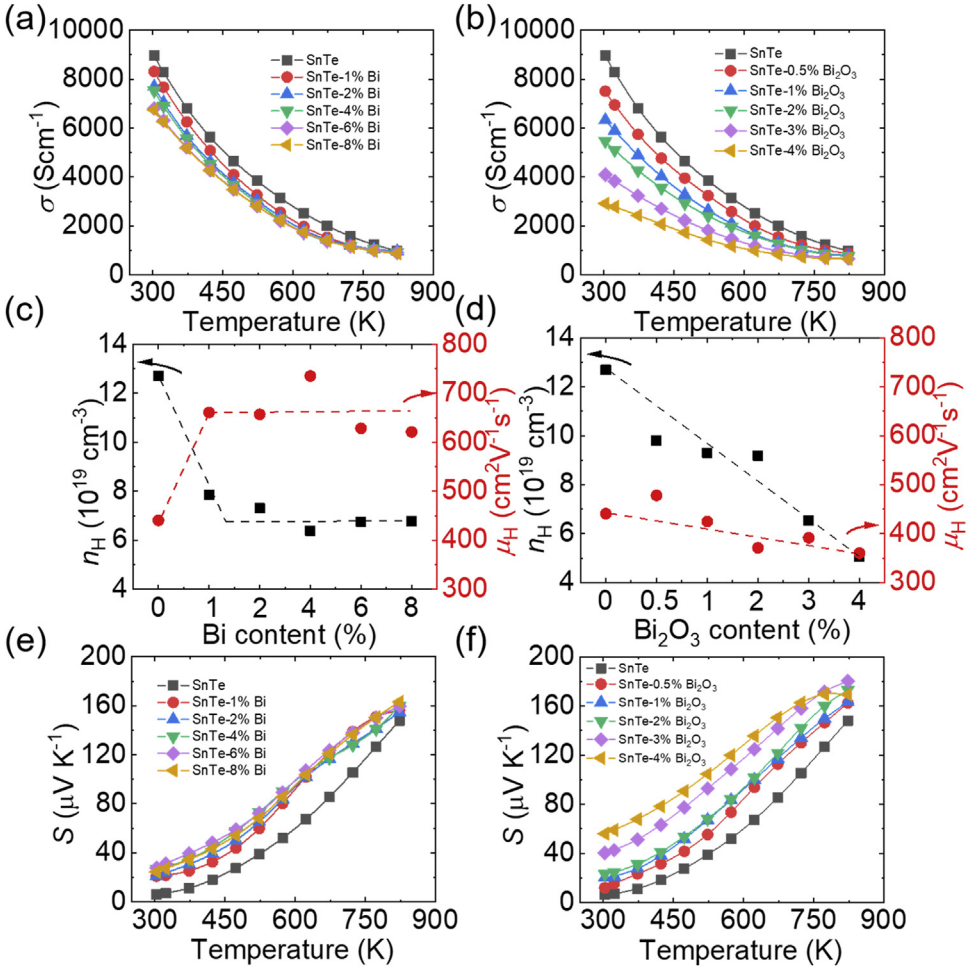

Fig. 2. The electrical conductivity of (a) SnTe-x% Bi (x = 0–8%) and (b) SnTe-y% Bi_2O_3 (y = 0–4%); the room-temperature carrier concentration and carrier mobility of (c) SnTe-x% Bi and (d) SnTe-y% Bi_2O_3; the Seebeck coefficient of (e) SnTe-x% Bi and (f) SnTe-y% Bi_2O_3.

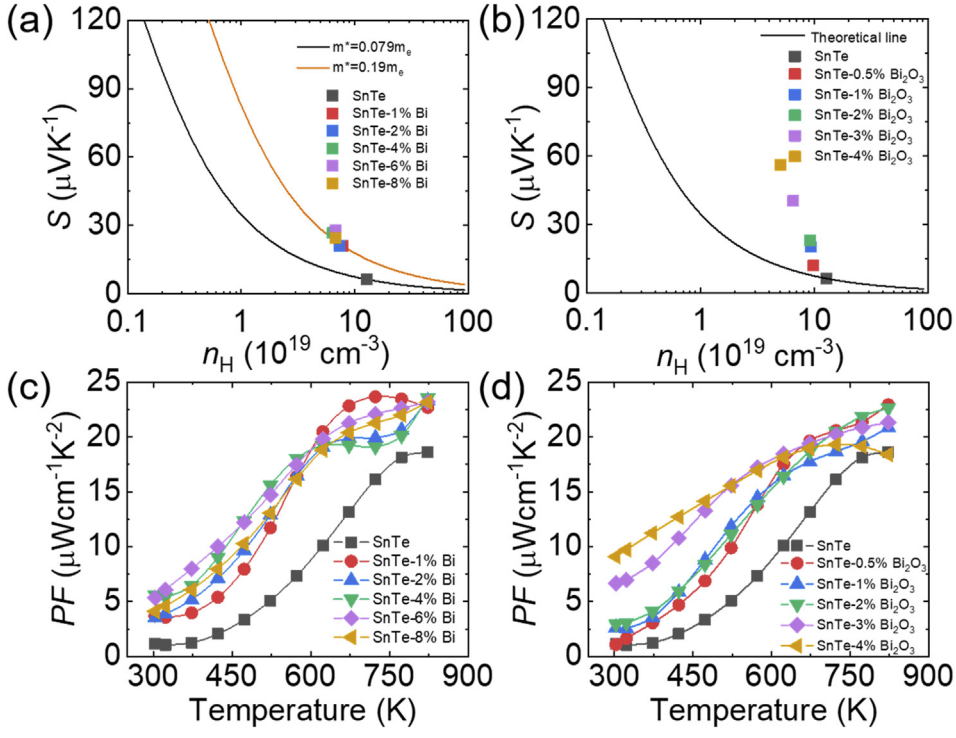

Fig. 3. The room-temperature Seebeck coefficients of (a) SnTe-x% Bi (x = 0–8%) and (b) SnTe-y% Bi_2O_3 (y = 0–4%) samples as a function of carrier concentration. The Pisarenko curves are based on the single parabolic band model, and the colored points are the experimental results; Power factor of (c) SnTe-x% Bi and (d) SnTe-y% Bi_2O_3.

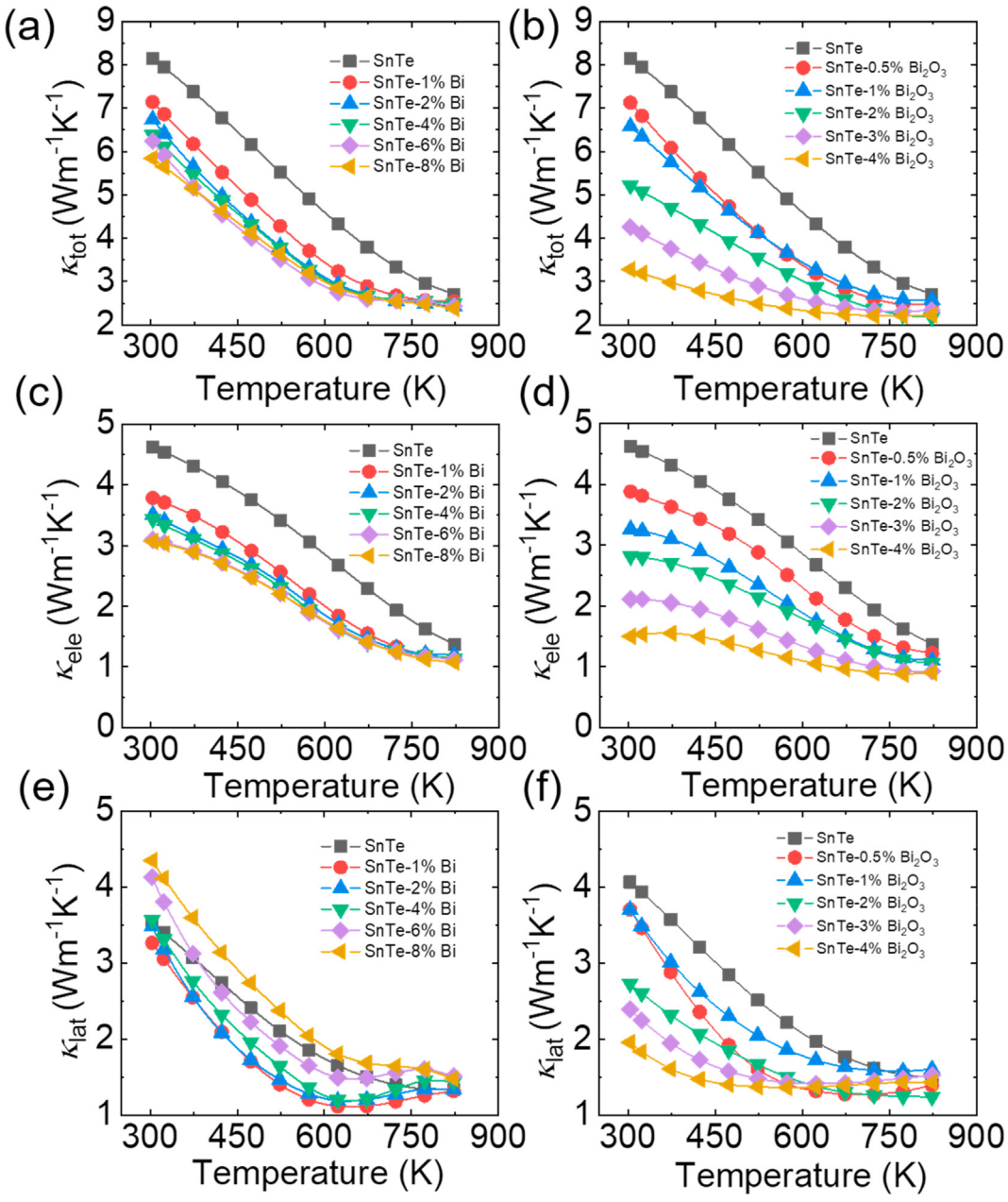

Fig. 4. The total thermal conductivity of (a) SnTe-x% Bi (x = 0–8%) and (b) SnTe-y% Bi_2O_3 (y = 0–4%); electronic thermal conductivity of (c) SnTe-x% Bi and (d) SnTe-y% Bi_2O_3; lattice thermal conductivity of (e) SnTe-x% Bi and (f) SnTe-y% Bi_2O_3.

in SnTe-x% Bi_2O_3 increased gradually with the rising Bi_2O_3 amount, which was much higher than the theoretically calculated curve, as shown in Fig. 3(b). Due to the high *S*, *PF* was improved from 18.6 μW cm^{-1} K^{-2} for pristine SnTe to 23.5 μW cm^{-1} K^{-2} for SnTe-8% Bi at 823 K. Nevertheless, SnTe-y% Bi_2O_3 obtained a larger average *PF* when y ≥ 3, especially, there was a pronounced boost from 1.1 μW cm^{-1} K^{-2} for SnTe to 9.0 μW cm^{-1} K^{-2} for SnTe-y% Bi_2O_3 at 300 K, as shown in Fig. 3(c, d).

Fig. 4 represents the thermal transport properties of SnTe-x% Bi and SnTe-y% Bi_2O_3 (Diffusivities and sample densities can be found in Fig. S3 and Table S1). The total thermal conductivity (κ_{tot}) decreased significantly with 1% Bi and then decreased slightly with rising Bi contents. However, κ_{tot} in SnTe-y% Bi_2O_3 decreased dramatically with rising Bi_2O_3 amounts. Specifically, κ_{tot} at room temperature reduced from 8.2 W m^{-1} K^{-1} for SnTe to 3.3 W m^{-1} K^{-1} for SnTe-4% Bi_2O_3, as shown in Fig. 4(a–b). To get an insight into the low κ_{tot}, we evaluated both κ_{ele} and κ_{lat}, according to $\kappa_{tot} = \kappa_{lat}+\kappa_{ele} = \kappa_{lat} + L\sigma T$, where *L* is the Lorenz number. We took the Lorenz number as a constant value of 1.7 × 10^{-8} W Ω K^{-1} due to the high n_H in SnTe. Fig. 4(c) shows that decreased κ_{tot} in SnTe-x% Bi was mainly from κ_{ele} decline. Nevertheless, the decreased κ_{tot} in SnTe-y% Bi_2O_3 came from the simultaneous reduction of both κ_{ele} and κ_{lat} in Fig. 4(d), originating from the reduced n_H and the enhanced phonon scattering, respectively. Fig. 4(e) represents the κ_{lat} trend changing with the temperature for SnTe-x% Bi. It can be easily noted that the κ_{lat} first decreased and then increased, and a strong bipolar diffusion was clearly observed at temperatures above 600 K. However, in Fig. 4(f), the κ_{lat} of SnTe-y% Bi_2O_3 kept decreasing. We could conclude that the Bi_2O_3 can also suppress the bipolar diffusion effect in SnTe due to the energy filtering effect.

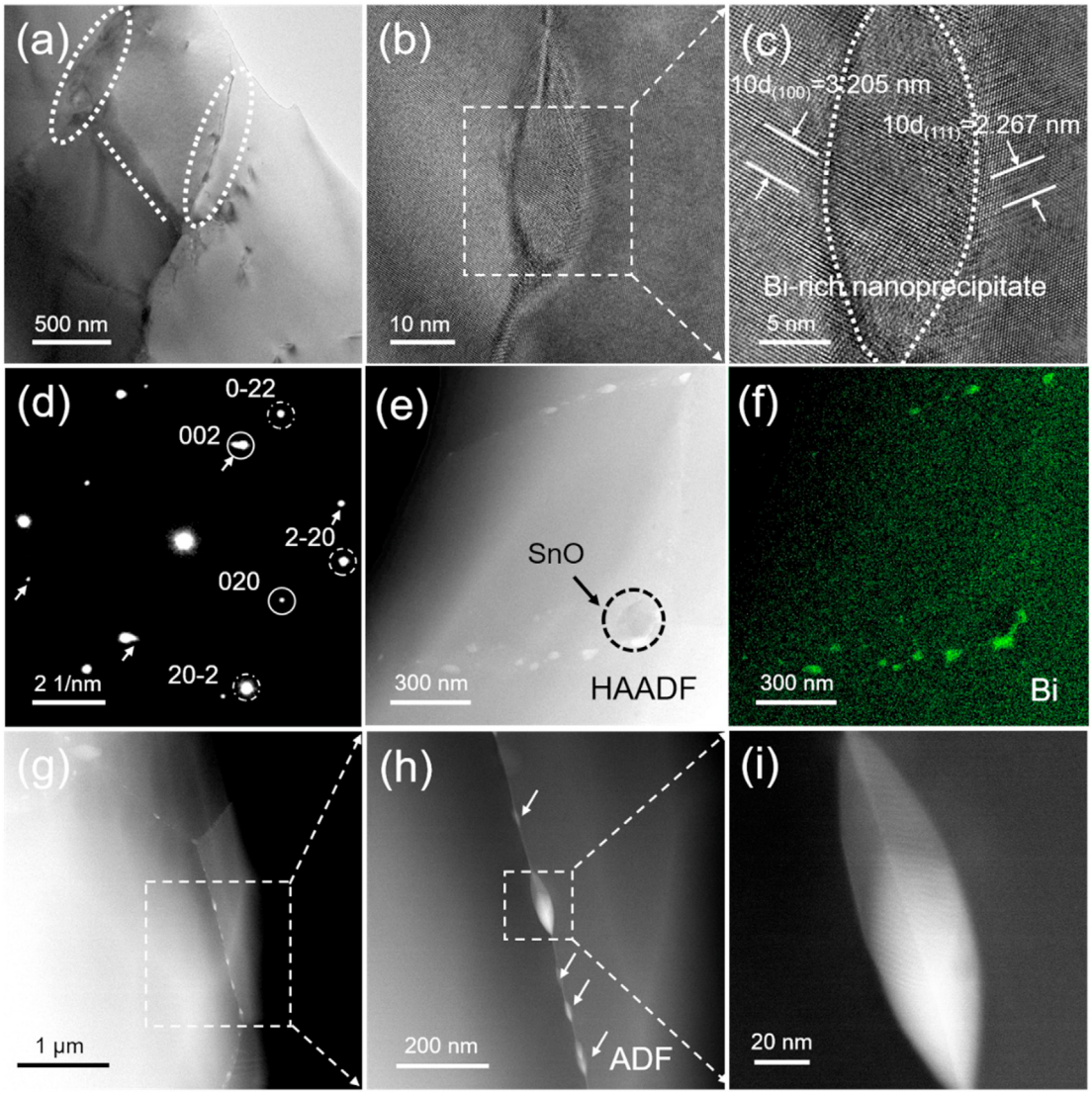

Fig. 5. The microstructure of the SnTe−3%Bi_2O_3 sample: (a) The low-magnification and (b) middle-magnification bright-field TEM images; (c) High-resolution TEM image of a selected nanoprecipitate and (d) the corresponding selected area electron diffraction pattern; (e) High angle annular dark-field STEM images and (f) the corresponding elemental mappings attained from the STEM energy-dispersive X-ray spectroscopy; (g–i) The HAADF distribution and morphology images of the nanoprecipitates at different magnifications.

To clarify the increase of S and the decrease of κ_{lat}, the SnTe−3% Bi_2O_3 sample was characterized by transmission electron microscopy (TEM). Fig. 5(a) shows the morphological image at low magnification, from which we can clearly see the presence of grain boundaries, nanoprecipitates, and some dislocation lines. These nanoprecipitates tended to distribute at the grain boundaries. Fig. 5(b) indicates one nanoprecipitate resided at the grain boundary with the medium magnification. Fig. 5(c) is the high-resolution TEM (HRTEM) image enlarged from Fig. 5(b) and (d) is the corresponding selected area electron diffraction (SAED). As shown in Fig. 5(c), the SnTe matrix on the left side of the nanoprecipitate was arranged along the [100] axis and the left side was along [111] direction, which was confirmed by the SAED image in Fig. 5(d). There were two sets of electron diffraction spots, representing the diffraction spots from the [100] axis (marked by the solid line circles) and [111] axis (marked by the dashed circles), respectively. Moreover, a split can be seen from (002) and (00-2) (marked by the solid circles).

To determine the composition and distribution of the nanoprecipitates, we analyzed the samples using the STEM mode. Fig. 5(e–i) show the images of the samples in HAADF mode and the elemental analysis maps. Fig. 5(e) shows the distribution of nanoprecipitates in the matrix. It can be seen that the nanoprecipitates were mainly distributed around the grain boundaries, with scales ranging from tens to hundreds of nanometers. The elemental analysis map in Fig. 5(f) clearly shows that these nanoprecipitates are Bi rich (the other elemental mappings were shown in Fig. S4). Fig. 5(g) indicates the distribution of the nanoprecipitates in a larger area. It can be found that all the nanoprecipitates were embedded at the grain boundaries instead of within the grain. Fig. 5(h–i) show that the nanoprecipitates were in a leaf-like shape. In the HAADF image, the nanoprecipitates were brighter than the SnTe matrix because of the element contrast difference. Accordingly, we concluded that the composition of the nanoprecipitates is Bi-rich.

Fig. 6(a) shows a schematic diagram of the energy filtering effect between the SnTe matrix and Bi_2O_3/SnO_2 nanoprecipitates [40–42]. Due to the high potential barrier at the valence band, this interface could effectively block the low-energy hole carrier while allowing the high energy carrier to pass through, leading to increased m^* [40,43]. As shown in Fig. 6(b) and (c), SnTe-y% Bi_2O_3

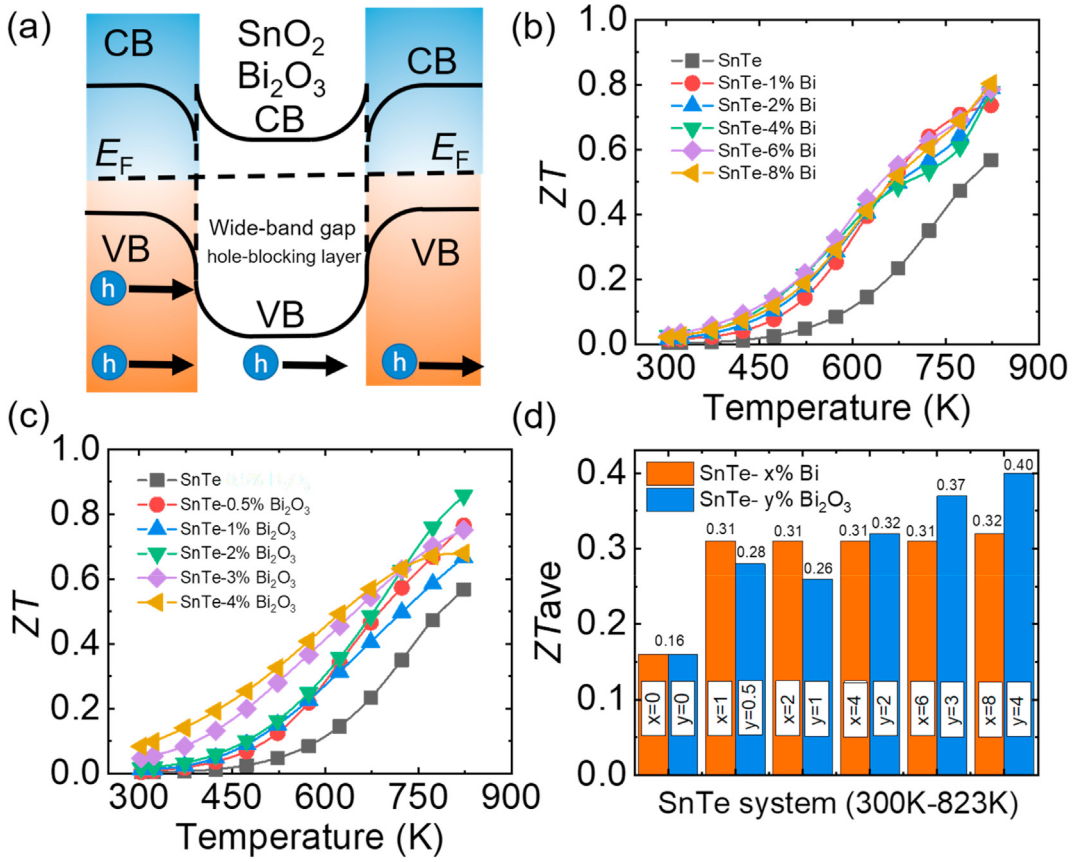

Fig. 6. (a) Schematic diagram of the carrier energy barrier at the interface between SnO_2 and SnTe and at the interface between Bi_2O_3 and SnTe; The *ZT* value of the (b) SnTe-x% Bi (x = 0–8%) and (c) SnTe-y% Bi_2O_3 (y = 0–4%) samples; (d) The calculated average *ZT* value in the range of 300 K–823 K.

has higher TE performance than SnTe-x% Bi, specifically at room temperature, because of the combined effect of the enhanced *S* and the reduced κ. Proving that the energy filtering effect plays a critical role in optimizing the TE properties of SnTe.

We also calculated ZT_{ave} of the samples by the following equation:

$$ZT_{ave} = \frac{1}{T_h - T_c}\int_{T_c}^{T_h} ZT dT \quad (1)$$

As shown in Fig. 6(d), ZT_{ave} of SnTe-x% Bi samples at 300–823 K was 0.31 and remained nearly constant when x $\geq$ 1, while ZT_{ave} of SnTe-y% Bi_2O_3 samples significantly increased with the rising Bi_2O_3 content, eventually reaching ~ 0.40 for SnTe-4% Bi_2O_3.

3. Conclusion

In this work, Bi and Bi_2O_3 were added to the SnTe matrix through high-temperature solid-phase reactions. By comparing SnTe-x% Bi and SnTe-y% Bi_2O_3, we found that SnTe-y% Bi_2O_3 presented superior TE performance than SnTe-x% Bi, which was derived from the SnO_2, Bi_2O_3, and Bi-rich nanoprecipitates. These interfaces between the SnTe matrix and Bi_2O_3/SnO_2 nanoprecipitates form a strong energy filtering effect to enhance the average *PF* through increasing *S*. Moreover, abundant and diverse nanoprecipitates can significantly diminish κ_{lat} through enhanced phonon scattering. The combined effects resulted in a ZT_{max} value of 0.9 for SnTe-2% Bi_2O_3 and a ZT_{ave} of 0.4 at 300–823 K for SnTe-4% Bi_2O_3. The work provides an excellent reference to develop non-toxic high-performance TE materials.

Author contributions

Tao Hong conceived and carried out the experiments, synthesized the samples, performed the SEM and TEM measurements with the assistance of Xiang Gao and wrote this paper. Changrong Guo conceived and carried out the experiments, synthesized the samples. Dongyang Wang conceived the experiments, analyzed the results and co-edited the manuscript. Bingchao Qin conceived the experiments, analyzed the results and co-edited the manuscript. Cheng Chang, Xiang Gao and Li-Dong Zhao designed and carried out the experiments, analyzed the results and co-edited the manuscript.

Declaration of competing interest

The authors declare that they have no known competing financial interests or personal relationships that could have appeared to influence the work reported in this paper.

Acknowledgments

This work was supported by National Natural Science Foundation of China (52002042), National Key Research and Development Program of China (2018YFA0702100 and 2018YFB0703600), 111 Project (B17002) and Lise Meitner Project M 2889-N. This work was also supported by the National Postdoctoral Program for Innovative Talents (BX20200028). L.D.Z. appreciates the support of the high-performance computing (HPC) resources at Beihang University, the National Science Fund for Distinguished Young Scholars

(51925101), and center for High Pressure Science and Technology Advanced Research (HPSTAR) for SEM and TEM measurements.

Appendix A. Supplementary data

Supplementary data to this article can be found online at https://doi.org/10.1016/j.mtener.2022.100985.

References

[1] B. Qin, D. Wang, L.D. Zhao, Slowing down the heat in thermoelectrics, InfoMat 3 (2021) 755–789, https://doi.org/10.1002/inf2.12217.

[2] G. Tan, L.D. Zhao, M.G. Kanatzidis, Rationally designing high-performance bulk thermoelectric materials, Chem. Rev. 116 (2016) 12123–12149, https://doi.org/10.1021/acs.chemrev.6b00255.

[3] X. Zhang, L.D. Zhao, Thermoelectric materials: energy conversion between heat and electricity, J. Materiomics 1 (2015) 92–105, https://doi.org/10.1016/j.jmat.2015.01.001.

[4] R. Moshwan, L. Yang, J. Zou, Z.G. Chen, Eco-friendly SnTe thermoelectric materials: progress and future challenges, Adv. Funct. Mater. 27 (2017) 201703278, https://doi.org/10.1002/adfm.201703278.

[5] Y. Xiao, L.D. Zhao, Seeking new, highly effective thermoelectrics, Science 367 (2020) 1196–1197, https://doi.org/10.1126/science.aaz9426.

[6] W.W. Qu, X.X. Zhang, B.F. Yuan, L.D. Zhao, Homologous layered $InFeO_3(ZnO)_m$: new promising abradable seal coating materials, Rare Met. 37 (2017) 79–94, https://doi.org/10.1007/s12598-017-0978-6.

[7] G.J. Snyder, E.S. Toberer, Complex thermoelectric materials, Nat. Mater. 7 (2008) 105–114, https://doi.org/10.1038/nmat2090.

[8] D. Wu, Y. Pei, Z. Wang, H. Wu, L. Huang, L.D. Zhao, J. He, Significantly enhanced thermoelectric performance in n-type heterogeneous BiAgSeS composites, Adv. Funct. Mater. 24 (2014) 7763–7771, https://doi.org/10.1002/adfm.201402211.

[9] X. Zhang, C. Chang, Y. Zhou, L.D. Zhao, BiCuSeO thermoelectrics: an update on recent progress and perspective, Materials 10 (2017) 198, https://doi.org/10.3390/ma10020198.

[10] X. Liu, D. Wang, H. Wu, J. Wang, Y. Zhang, G. Wang, S.J. Pennycook, L.D. Zhao, Intrinsically low thermal conductivity in $BiSbSe_3$: a promising thermoelectric material with multiple conduction bands, Adv. Funct. Mater. 29 (2019) 1806558, https://doi.org/10.1002/adfm.201806558.

[11] Y. Qiu, Y. Jin, D. Wang, M. Guan, W. He, S. Peng, R. Liu, X. Gao, L.D. Zhao, Realizing high thermoelectric performance in GeTe through decreasing the phase transition temperature via entropy engineering, J. Mater. Chem. A 7 (2019) 26393–26401, https://doi.org/10.1039/c9ta10963c.

[12] C. Chang, D. Wang, D. He, W. He, F. Zhu, G. Wang, J. He, L.D. Zhao, Realizing high ranged out of plane ZTs in n type SnSe crystals through promoting continuous phase transition, Adv. Energy Mater. 9 (2019) 1901334, https://doi.org/10.1002/aenm.201901334.

[13] C. Chang, G. Tan, J. He, M.G. Kanatzidis, L.D. Zhao, The thermoelectric properties of SnSe continue to surprise: extraordinary electron and phonon transport, Chem. Mater. 30 (2018) 7355–7367, https://doi.org/10.1021/acs.chemmater.8b03732.

[14] R.F. Brebrick, A.J. Strauss, Anomalous thermoelectric power as evidence for two-valence bands in SnTe, Phys. Rev. 131 (1963) 104–110, https://doi.org/10.1103/PhysRev.131.104.

[15] L.M. Rogers, Valence band structure of SnTe, J. Phys. D 1 (1968) 845–852, https://doi.org/10.1088/0022-3727/1/7/304.

[16] B.C. Qin, Y. Xiao, Y.M. Zhou, L.D. Zhao, Thermoelectric transport properties of Pb–Sn–Te–Se system, Rare Met. 37 (2017) 343–350, https://doi.org/10.1007/s12598-017-0991-9.

[17] Y. Xiao, D. Wang, B. Qin, J. Wang, G. Wang, L.D. Zhao, Approaching topological insulating states leads to high thermoelectric performance in n-Type PbTe, J. Am. Chem. Soc. 140 (2018) 13097–13102, https://doi.org/10.1021/jacs.8b09029.

[18] F. Guo, B. Cui, Y. Liu, X. Meng, J. Cao, Y. Zhang, R. He, W. Liu, H. Wu, S.J. Pennycook, W. Cai, J. Sui, Thermoelectric SnTe with band convergence, dense dislocations, and interstitials through Sn Self-compensation and Mn alloying, Small 14 (2018) 201802615, https://doi.org/10.1002/smll.201802615.

[19] Z. Zhou, J. Yang, Q. Jiang, Y. Luo, D. Zhang, Y. Ren, X. He, J. Xin, Multiple effects of Bi doping in enhancing the thermoelectric properties of SnTe, J. Mater. Chem. A 4 (2016) 13171–13175, https://doi.org/10.1039/c6ta04240f.

[20] A. Banik, B. Vishal, S. Perumal, R. Datta, K. Biswas, The origin of low thermal conductivity in $Sn_{1-x}Sb_xTe$: phonon scattering via layered intergrowth nanostructures, Energy Environ. Sci. 9 (2016) 2011–2019, https://doi.org/10.1039/c6ee00728g.

[21] J. He, J. Xu, G.-Q. Liu, H. Shao, X. Tan, Z. Liu, J. Xu, H. Jiang, J. Jiang, Enhanced thermopower in rock-salt SnTe-CdTe from band convergence, RSC Adv. 6 (2016) 32189–32192, https://doi.org/10.1039/c6ra02658c.

[22] W. Li, Z. Chen, S. Lin, Y. Chang, B. Ge, Y. Chen, Y. Pei, Band and scattering tuning for high performance thermoelectric $Sn_{1-x}Mn_xTe$ alloys, J. Materiomics 1 (2015) 307–315, https://doi.org/10.1016/j.jmat.2015.09.001.

[23] T.Z. Fu, J.Z. Xin, T.J. Zhu, J.J. Shen, T. Fang, X.B. Zhao, Approaching the minimum lattice thermal conductivity of p-type SnTe thermoelectric materials by Sb and Mg alloying, Sci. Bull. 64 (2019) 1024–1030, https://doi.org/10.1016/j.scib.2019.06.007.

[24] Y.-L. Pei, H. Wu, J. Sui, J. Li, D. Berardan, C. Barreteau, L. Pan, N. Dragoe, W.S. Liu, J. He, L.D. Zhao, High thermoelectric performance in n-type BiAgSeS due to intrinsically low thermal conductivity, Energy Environ. Sci. 6 (2013) 1750, https://doi.org/10.1039/c3ee40879e.

[25] W. He, D. Wang, J.-F. Dong, Y. Qiu, L. Fu, Y. Feng, Y. Hao, G. Wang, J. Wang, C. Liu, J.-F. Li, J. He, L.D. Zhao, Remarkable electron and phonon band structures lead to a high thermoelectric performance ZT > 1 in earth-abundant and eco-friendly SnS crystals, J. Mater. Chem. A 6 (2018) 10048–10056, https://doi.org/10.1039/c8ta03150a.

[26] S.H. Yang, T.J. Zhu, T. Sun, J. He, S.N. Zhang, X.B. Zhao, Nanostructures in high-performance $(GeTe)_x(AgSbTe_2)_{100-x}$ thermoelectric materials, Nanotechnology 19 (2008) 245707, https://doi.org/10.1088/0957-4484/19/24/245707.

[27] A. Banik, K. Biswas, Lead-free thermoelectrics: promising thermoelectric performance in p-type $SnTe_{1-x}Se_x$ system, J. Mater. Chem. A 2 (2014) 9620–9625, https://doi.org/10.1039/c4ta01333f.

[28] Y. Pei, L. Zheng, W. Li, S. Lin, Z. Chen, Y. Wang, X. Xu, H. Yu, Y. Chen, B. Ge, Interstitial point defect scattering contributing to high thermoelectric performance in SnTe, Adv. Electron. Mater. 2 (2016) 201600019, https://doi.org/10.1002/aelm.201600019.

[29] X. Qian, H. Wu, D. Wang, Y. Zhang, J. Wang, G. Wang, L. Zheng, S.J. Pennycook, L.D. Zhao, Synergistically optimizing interdependent thermoelectric parameters of n-type PbSe through alloying CdSe, Energy Environ. Sci. 12 (2019) 1969–1978, https://doi.org/10.1039/c8ee03386b.

[30] G. Tan, L.D. Zhao, F. Shi, J.W. Doak, S.H. Lo, H. Sun, C. Wolverton, V.P. Dravid, C. Uher, M.G. Kanatzidis, High thermoelectric performance of p-type SnTe via a synergistic band engineering and nanostructuring approach, J. Am. Chem. Soc. 136 (2014) 7006–7017, https://doi.org/10.1021/ja500860m.

[31] K. Biswas, J. He, I.D. Blum, C.I. Wu, T.P. Hogan, D.N. Seidman, V.P. Dravid, M.G. Kanatzidis, High-performance bulk thermoelectrics with all-scale hierarchical architectures, Nature 489 (2012) 414–418, https://doi.org/10.1038/nature11439.

[32] Y. Pei, G. Tan, D. Feng, L. Zheng, Q. Tan, X. Xie, S. Gong, Y. Chen, J.F. Li, J. He, M.G. Kanatzidis, L.D. Zhao, Integrating band structure engineering with all-scale hierarchical structuring for high thermoelectric performance in PbTe system, Adv. Energy Mater. 7 (2017) 201601450, https://doi.org/10.1002/aenm.201601450.

[33] G. Tan, F. Shi, S. Hao, H. Chi, L.D. Zhao, C. Uher, C. Wolverton, V.P. Dravid, M.G. Kanatzidis, Codoping in SnTe: enhancement of thermoelectric performance through synergy of resonance levels and band convergence, J. Am. Chem. Soc. 137 (2015) 5100–5112, https://doi.org/10.1021/jacs.5b00837.

[34] G. Tan, F. Shi, J.W. Doak, H. Sun, L.D. Zhao, P. Wang, C. Uher, C. Wolverton, V.P. Dravid, M.G. Kanatzidis, Extraordinary role of Hg in enhancing the thermoelectric performance of p-type SnTe, Energy Environ. Sci. 8 (2015) 267–277, https://doi.org/10.1039/c4ee01463d.

[35] L.D. Zhao, X. Zhang, H. Wu, G. Tan, Y. Pei, Y. Xiao, C. Chang, D. Wu, H. Chi, L. Zheng, S. Gong, C. Uher, J. He, M.G. Kanatzidis, Enhanced thermoelectric properties in the counter-doped SnTe system with strained endotaxial SrTe, J. Am. Chem. Soc. 138 (2016) 2366–2373, https://doi.org/10.1021/jacs.5b13276.

[36] Z. Zhou, J. Yang, Q. Jiang, D. Zhang, J. Xin, X. Li, Y. Ren, X. He, Thermoelectric performance of SnTe with ZnO carrier compensation, energy filtering, and multiscale phonon scattering, J. Am. Chem. Soc. 100 (2017) 5723–5730, https://doi.org/10.1111/jace.15088.

[37] T. Hong, D. Wang, B. Qin, X. Zhang, Y. Chen, X. Gao, L.D. Zhao, Band convergence and nanostructure modulations lead to high thermoelectric performance in $SnPb_{0.04}Te$-y% $AgSbTe_2$, Mater. Today Phys. 21 (2021) 100505, https://doi.org/10.1016/j.mtphys.2021.100505.

[38] G. Tan, F. Shi, H. Sun, L.D. Zhao, C. Uher, V.P. Dravid, M.G. Kanatzidis, SnTe-$AgBiTe_2$ as an efficient thermoelectric material with low thermal conductivity, J. Mater. Chem. A 2 (2014) 20849–20854, https://doi.org/10.1039/c4ta05530f.

[39] J. He, J. Xu, X. Tan, G.-Q. Liu, H. Shao, Z. Liu, H. Jiang, J. Jiang, Synthesis of SnTe/$AgSbSe_2$ nanocomposite as a promising lead-free thermoelectric material, J. Materiomics 2 (2016) 165–171, https://doi.org/10.1016/j.jmat.2016.05.001.

[40] D. Narducci, E. Selezneva, G. Cerofolini, S. Frabboni, G. Ottaviani, Impact of energy filtering and carrier localization on the thermoelectric properties of granular semiconductors, J. Solid State Chem. 193 (2012) 19–25, https://doi.org/10.1016/j.jssc.2012.03.032.

[41] T.H. Liu, J.W. Zhou, M.D. Li, Z.W. Ding, Q.C. Song, B.L. Liao, L. Fu, G. Chen, Electron mean-free-path filtering in Dirac material for improved thermoelectric performance, Proc. Natl. Acad. Sci. U.S.A. 115 (2018) 879–884, https://doi.org/10.1073/pnas.1715477115.

[42] C. Gayner, Y. Amouyal, Energy filtering of charge carriers: current trends, challenges, and prospects for thermoelectric materials, Adv. Funct. Mater. 30 (2020) 201901789, https://doi.org/10.1002/adfm.201901789.

[43] Z. Ma, C. Wang, J. Lei, D. Zhang, Y. Chen, Y. Wang, J. Wang, Z. Cheng, Core-shell nanostructures introduce multiple potential barriers to enhance energy filtering for the improvement of the thermoelectric properties of SnTe, Nanoscale 12 (2020) 1904–1911, https://doi.org/10.1039/c9nr09331a.